Available online at www.sciencedirect.com
ScienceDirect
International Journal of Mass Spectrometry 265 (2007) 146–158
International Journal of Mass Spectrometry
www.elsevier.com/locate/ijms

Vacuum electrospray ionization study of the ionic liquid, [Emim][Im]

Y.-H. Chiu [a,*], G. Gaeta [a,1], D.J. Levandier [b], R.A. Dressler [a,*], J.A. Boatz [c]

[a] *Air Force Research Laboratory, Space Vehicles Directorate, Hanscom AFB, MA 01731-3010, USA*
[b] *Institute for Scientific Research, Boston College, Chestnut Hill, MA 02159, USA*
[c] *Air Force Research Laboratory, Propulsion Directorate, Edwards AFB, CA 93524, USA*

Received 21 November 2006; received in revised form 1 February 2007; accepted 7 February 2007
Available online 14 February 2007

Abstract

An analysis is presented of positive and negative vacuum electrospray currents from the ionic liquid, [Emim][Im], wetted on a sharp tungsten needle. The source is operated in a cone–jet configuration established with a low extraction voltage of approximately ±1 kV. Emission current and mass flow are measured as a function of the emitter angle with respect to the instrument axis. Mass spectra of field evaporated ions and mass-resolved energy distributions of emitted charges are recorded as a function of emitter angle. The measurements at both source polarities indicate that the cone–jet emits a mixture of ions and charged droplets. While the charged droplets are emitted with a narrow angular distribution centered on axis, the angular distributions of ions are significantly broader than those of the droplets and centered off axis. Pure ion emission is observed at emission angles larger than ∼15°. The main mass spectral peaks are from $X^{\pm}\{[Emim][Im]\}_n$ ions (X = Emim or Im for positive and negative polarities, respectively) with $n = 0$, 1, and 2. Quantum chemical calculations of the $n = 0$ and 1 ions and the isolated ion pairs are presented, yielding thermochemical information on the observed ionic species. The present results demonstrate that the cone–jet emits droplets from the tip of the jet, and provide direct evidence that ions are produced in an Iribarne–Thomson field-evaporation mechanism at the transition region between the Taylor cone and jet. Electrochemical modification of the cone–jet emitter properties are observed when maintaining the emitter at a positive polarity for a prolonged (minutes to hours) period. New ions emerge consisting of clusters containing a neutralized Im^-. The associated current suppression can be mitigated through polarity alternation at 1 Hz. Measurements are also presented with the tungsten needle heated to 373 K, thereby reducing the liquid viscosity and increasing the flow rate. The average mass of the droplets is observed to increase with temperature while the mass distributions of the ions are not found to change noticeably.
Published by Elsevier B.V.

Keywords: Electrospray; Ionic liquid; Taylor cone; Electrochemistry; Ethyl-methyl-imidazolium ion

1. Introduction

Electrospray ionization (ESI) in conjunction with mass spectrometry most commonly involves electrospraying a sample in a volatile solvent at atmospheric pressure, and drawing the ions, released by droplets through a field evaporation mechanism outlined by Iribarne and Thomson [1,2], into the vacuum of a mass spectrometer through an atmosphere–vacuum interface. Prior to the work of Fenn et al. [3], considerable work had been conducted on ESI of liquids in a vacuum [4–6]. Formerly referred to as electrohydrodynamic ionization, the studies were limited to non-volatile solvents such as glycerol. Given the restricted choice of solvents and the resulting limited analytical utility, much of this work was discontinued in the late 1970s. A number of applications, including spacecraft electric propulsion [7], electrospinning [8], and new methods of drug delivery [9] have called for an improved understanding of the detailed physics associated with ESI jets. This has instigated a revival of vacuum ESI research.

In the electrohydrodynamic ionization experiments of the late 1960s and 1970s, the applied extraction voltage was very high, exceeding 5 kV. The high resulting local fields generated a stressed jet regime leading to multiple jets on the rim of the capillary orifice [10]. At lower extraction voltages just above the electrospray threshold, charge emission occurs from a single jet in a more readily characterizable configuration referred to as a cone–jet, schematically depicted in Fig. 1A. The cone–jet can be divided into 3 regions, the cone region, referred to as the

* Corresponding authors.
E-mail address: Yu-Hui.Chiu@Hanscom.af.mil (Y.-H. Chiu).
[1] Present address: Space Systems/Loral, 3825 Fabian Way, M/S G.86, Palo Alto, CA 94303, USA.

1387-3806/$ – see front matter. Published by Elsevier B.V.
doi:10.1016/j.ijms.2007.02.010

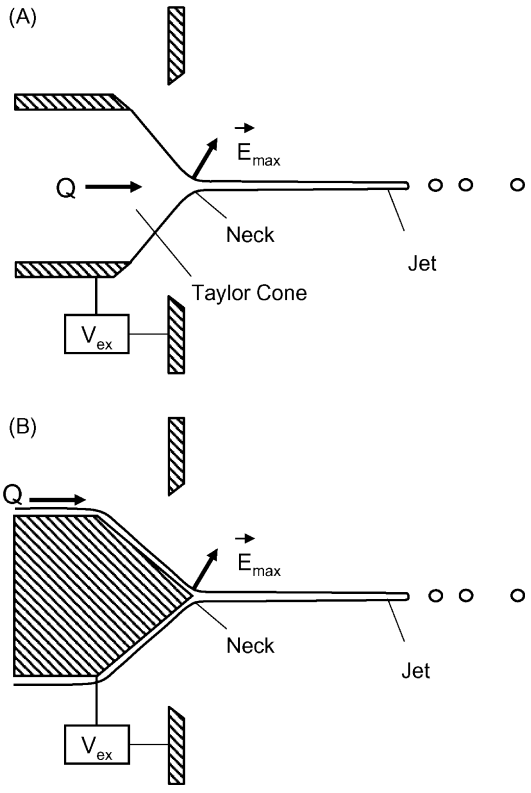

Fig. 1. (A) Schematic representation of a cone–jet associated with a conducting liquid emerging from a capillary and subjected to a high electric field. (B) Cone–jet formation on an externally wetted sharp needle tip.

Taylor cone due to the work by Taylor [11], the intermediate neck region, and the jet, which eventually breaks up into charged droplets. The current density increases as the apex of the Taylor cone is approached. In the jet, the current is convective and the charge density decreases as the jet flow accelerates towards the point of droplet formation. Thus, the region of highest charge density and ohmic current is the transition neck region. Gamero-Castaño and Fernández de la Mora [12] showed that the maximum surface-normal electric field and radius of curvature, or jet radius, at the neck are given by:

$$E_{\max} = \frac{\gamma^{1/2}}{\varepsilon_0^{2/3}} \left(\frac{K}{Q}\right)^{1/6}, \quad (1)$$

$$R_{\max} = \left[\frac{\varepsilon_0 Q}{K}\right]^{1/3}, \quad (2)$$

where K and ε_0 are the liquid conductivity and permittivity of vacuum, respectively, γ is the surface tension of the liquid, and Q is the volume flow rate. They demonstrated for the first time that the flow rate of a concentrated NaI/formamide solution could be reduced to the point that $E_{\max}$ exceeded 1 V/nm. Surface-normal field strengths on the order of 1 V/nm are known to be a threshold value for ion field evaporation from liquids [2,13–15]. For volume flow rates of less than 100 pl/s at solution conductivities exceeding 1 S/m, Gamero-Castaño and Fernández de la Mora [12] observed ion currents that exceeded the charged droplet current. At these conditions, the curvature of the transition region and the diameter of the jet are predicted to be in the vicinity of 10 nm. In a combined retarding potential and time-of-flight analysis, Gamero-Castaño [16] determined that the charged droplets were produced with energies per charge approximately 200 V lower than the particles produced at the emitter potential, and that ions were at similar energies per charge with a tail towards lower energies and only a minor contribution at higher energies. With the assumption that ohmic losses occur primarily in the cone–neck region, the observations of Gamero-Castaño [16] suggest that the field evaporated ions are primarily produced downstream from the neck, most likely at the jet tip where droplet fission occurs. This contradicts the electrohydrodynamic predictions outlined by Gamero-Castaño and Fernández de la Mora [12] that predicts ion field evaporation at the neck. The results of Gamero-Castaño have been confirmed by mass spectrometric measurements by Chiu et al. [17].

More recently, the study of vacuum ESI has been further revitalized through the emergence of novel ionic liquids. Their negligible vapor pressures and significant conductivities make them ideal candidates for electrospray space propulsion systems, as first proposed by Fernández de la Mora and later reported in [18]. The title ionic liquid, 1-ethyl-3-methylimidazolium *bis*(trifluoromethylsulfonyl)imide ([Emim][Im]), is the propellant earmarked for an electrospray propulsion system of an upcoming high-precision positioning demonstration, the Jet Propulsion Laboratory ST7 Disturbance Reduction System experiment [19]. Adding additional flexibility to ESI source designs and space propulsion systems, Lozano and Martinez-Sanchez have shown that due to their negligible vapor pressure, ionic liquids can be readily sprayed in a vacuum from externally wetted sharp metal needle tips, as schematically shown in Fig. 1B [20].

While it is conceivable that electrolyte solutions, such as the formamide solution mentioned above, no longer behave like continuum charge fluids when the jet dimensions are small enough to reduce the ion populations in the transition region to isolated ions, ionic liquids should maintain charge fluid characteristics at much smaller dimensions. Thus, the study of [Emim][Im] in a mixed-ion/droplet field evaporation mode could provide verification of electrohydrodynamic predictions not confirmed by the formamide solutions. A first report from this laboratory [21] on the propulsion characteristics of [Emim][Im] when electrosprayed from a wetted tungsten tip, in fact, clearly demonstrates that field evaporation, as postulated by Iribarne and Thomson for charged droplets [1], occurs in the neck region of the cone–jet, as predicted by Gamero-Castaño and Fernández de la Mora [12,16]. Particularly important in the earlier study was the experimental ability to measure mass-resolved ion energy distributions, as well as mass-resolved angular distributions with respect to the emitter needle axis.

In this paper, we provide a detailed electrohydrodynamic and mass spectral analysis of the electrosprayed currents from [Emim][Im] wetted on a sharp tungsten tip, with specific focus on the properties of the nanodimensional spray. The present study also includes an investigation of the effects of heating the ionic liquid, a more thorough description of effects attributable

to electrochemical degradation of the ionic liquid, and a density functional theory thermochemical analysis of the observed ions in the mass spectrum.

2. Experimental

The mass spectrometric apparatus has been described in detail previously [21], and only a brief description will be given here. A wetted needle approach is used, as introduced by Lozano and Martinez-Sanchez [20], and schematically shown in Fig. 1B. The electrospray source consists of a tungsten tip with ∼20 μm curvature, electrochemically etched from a 500 μm diameter tungsten wire, and a drop of [Emim][Im] (Sigma–Aldrich, ≥97.0%) immobilized on a wire junction approximately 3 mm upstream from the tip. The liquid flows towards the tip from the droplet via capillary flow assisted by the roughness of the surface. The tip is positioned in the aperture of an extractor electrode with an orifice of 1.5 mm diameter. The emitter can be heated, and the source assembly consisting of emitter and extraction electrode can rotate with respect to the emitter tip origin in a plane parallel to the main axis of the apparatus. Thus, angular distributions of ion emission from cone–jets are possible. The tip and extraction optics are all in a vacuum (10^{-7} Torr). Typical extractor voltages used for [Emim][Im] were ±1.05 kV. Lozano and Martinez-Sanchez [22] have shown that indefinite operation is possible if the emitter polarity is alternated at a frequency sufficiently large to prevent formation of the electrochemical double layer on the emitter. This eliminates electrochemical processes and the associated degradation of the ionic liquid. For the present source, a polarity alternation at 1 Hz was sufficient to provide stable operation. The bias potentials applied to the tungsten tip were ±500 V, while the extractor was biased at ∓550 V for positive and negative polarity, respectively. These voltages were chosen to minimize the ion energy in the mass filter, while maintaining reasonable ion transmission through the apparatus. At absolute emitter biases of ∼500 V and below, sputtering on the quartz-crystal microbalance is shown to be relatively low.

The charged particle beam extracted from the tungsten tip can either be focused on a near-field target consisting of an interchangeable Faraday cup with an entrance aperture of 6 mm, a quartz crystal microbalance (QCM; XTM/2, Inficon) with aperture of the same size, or a cylindrical lens element for beam transmission. The near-field target is used for general characterization of the charged-particle beam through total current and mass flow measurements. The ratio between mass flow and current provides the average m/q value of emitted charges, which, in conjunction with mass spectrometric measurements, provides a measure of the fraction of charged droplets in the beam. When the cylindrical lens element is placed on-axis, the beam passes a 3 mm diameter aperture, after which the beam is focused and injected into a quadrupole mass filter. The solid angle of acceptance is ∼6°. Following transmission through the quadrupole, the ions pass through a retarding potential analyzer prior to being detected using an off-axis channeltron electron multiplier. The retarding potential analyzer is used to measure the energy distribution of mass-selected ions.

3. Computational methods

The geometries of the ethylmethylimidazolium cation ($Emim^+$), the *bis*(trifluoromethylsulfonyl)imide anion ($Im^- = [N(SO_2CF_3)_2]^-$), their corresponding neutral spin-doublet radicals ($Emim^0$ and Im^0, respectively), and the set of ion clusters $(Emim^0)(Im^-)$, $(Emim^+)(Im^0)$, $(Emim^+)_m(Im^-)_n$ $(0 \le m, n \le 2)$ were fully optimized at the density functional theory level using the B3LYP hybrid functional [23–25], which included the VWN5 correlation functional [26]. Since the potential energy surfaces of the ion clusters are quite "flat", more stringent convergence criteria were chosen for the geometry optimizations to ensure that true local minima were obtained. The specific criteria chosen for convergence of the optimized geometries were (a) the magnitude of each cartesian component of the gradient vector less than 10^{-5} Hartrees/Bohr and (b) the root mean square of the gradient vector norm less than 3.4×10^{-6} Hartrees/Bohr. The numerical grid consisted of 96 radial grid points in the Euler–Maclaurin quadrature and 36 theta angle points plus 72 phi angle points in the Gauss–Legendre quadrature.

Restricted open-shell Hartree–Fock (ROHF) methods were employed in the calculations of all spin doublet species. All structures were verified as local minima via diagonalization of the matrix of energy second derivatives; i.e., the Hessian matrix. All calculations were performed using the 6-31++G(d,p) basis set [27–29] and the GAMESS [30,31] quantum chemistry program.

4. Results

4.1. Electrospray experiments

Table 1 lists parameters derived from the near-field target (current and mass flow sensors) measurement for an emitter at room temperature and heated to 373 K (100 °C). The extraction voltage, V_{ex}, is the difference between emitter and extraction electrode potentials. The total emission current, I_0, is determined from an electrometer measurement in the emitter power supply biasing circuit. The comparison between I_0 and I_F, the Faraday cup current, provides a measure of the beam divergence. I_F

Table 1
Cone–jet parameters determined for [Emim][Im] wetted on a tungsten emitter

T (K)	300		373	
K (S/m)	0.88		3.5	
V_{ex} (V)	−1,050	1,050	−925	925
Polarity	+	−	+	−
I_0 (nA)	65.4	54.2	114	108
I_F (nA)	29.6	28.6	30	34
$\dot{m}$(QCM) (ng s^{-1})	7.5	5.0	27.3	22.6
m/q (Daltons)	24,200	16,900	86,700	64,200
E_{max} (V/nm)	1.0	1.1	1.05	1.1
R_{max} (nm)	3.7	3.3	3.6	3.4

K is the temperature dependent conductivity; V_{ex} the extraction voltage; I_0 and I_F correspond to the total emission and Faraday cup currents, respectively; $\dot{m}$(QCM) the mass flow as measured on the QCM; E_{max} and R_{max} correspond to the maximum electric field strength and the associated radius of curvature at the jet neck given by Eqs. (1) and (2).

and the mass flow, $\dot{m}$, recorded with the QCM deposition meter are listed for axial emission (zero emission angle). The average charged particle mass-to-charge ratio on axis is then given by: $m/q = \dot{m}/I_F$. E_{max} and R_{max} are derived from Eqs. (1) and (2) assuming a density of 1.52 g cm^{-3} for [Emim][Im] and surface tension, γ, of 0.0352 N m^{-1} for both temperatures [32].

The temperature has two effects on the ionic liquid: it raises the conductivity and lowers the viscosity. This is reflected in a number of measured parameters in Table 1. First, the extraction voltage necessary for stable cone–jet emission is significantly lower for the heated emitter. The total emission currents and the mass flow registered by the QCM deposition meter are significantly higher in the heated case. Heating also appears to produce a more divergent spray.

The large average m/q values suggest that the cone–jets emit in a mixed droplet/ion regime, where the main fraction of mass flow is carried by the droplets, while a substantial fraction of the current comes from ions. Thus, the present experiment operates in the regime where ion field evaporation occurs. This is verified by the derived values for E_{max} and R_{max}, which do not appear to depend on the temperature, i.e., K/Q remains constant when heating the ionic liquid from room temperature to 373 K. It must be kept in mind when evaluating the field and dimension values for high temperatures that no information on the density, and more importantly, the surface tension at 373 K was available at the time of writing this report.

Fig. 2 shows the angular dependence of $\dot{m}$ and I_F for the two polarities at the two temperatures. Except for different mass flow amplitudes for the different temperatures, the distributions are very similar in all cases, and indicate a narrower angular distribution for the mass flow in comparison with the current. The comparison between $\dot{m}$ and I_F demonstrates that there is significant current at large angles associated with negligible mass flow, signifying nearly pure ion emission. The ion currents do not depend greatly on temperature. At both temperatures and polarities, it can be seen that the deposition meter indicates negative mass flow near the wings of the distribution. In the high-temperature case the plot needs to be expanded in order to observe this. Since the negative mass flow is at an angle where ion currents are high, it is attributed to sputtering of deposited material. This is consistent with the increase of sputtering rates with q/m and the associated increase in impact energy.

The shown distributions are raw experimental data and do not represent azimuthally integrated values. Thus, it is important to note that the sensitivity drops proportional to sin(α), where α is the angle between the emitter and apparatus axes. Consequently, significant current at angles beyond 30° is possible.

Fig. 3 shows positive ion mass spectra recorded with the emitter needle parallel to and pointing down the instrument axis (on-axis) and at an angle of 20° between the emitter needle and instrument axes, for both temperatures. Note that the accuracy in the mass determination is ±4 amu due to the limited number of data points. The mass spectra are plotted on the same intensity scale for comparison. The most abundant positive ion masses, 110 ± 4, 500 ± 4, and 894 ± 4 amu, can be attributed to Emim$^+$([Emim][Im])$_n$, n = 0, 1, 2 (111, 502, and 893 amu, respectively). Minor trace positive ions with masses of 78, 148,

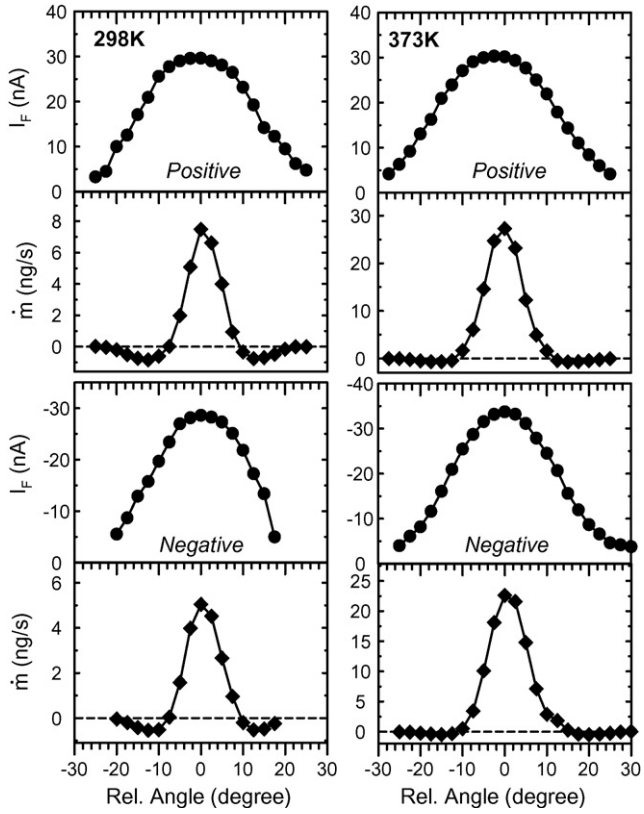

Fig. 2. Near-field target measurements of Faraday cup current (I_F) and mass flow ($\dot{m}$) as a function of the angle between the emitter axis and the main instrument axis. Measurements for positive and negative polarities at emitter temperatures of room temperature and 373 K are shown.

and 283 amu are also observed on-axis. The on-axis mass spectrum exhibits a persistent background while the 20° spectrum does not exhibit any measurable background. There are only minor differences between the corresponding spectra at room temperature and 373 K.

Fig. 4 shows the negative ion mass spectra observed on-axis and at 20°. The most abundant negative ion masses, 280 ± 4, 670 ± 4, and 1060 ± 4 amu can be attributed to Im$^-$([Emim][Im])$_n$, n = 0, 1, 2 (280, 671, and 1062 amu, respectively). Minor trace negative ions with masses of 87 and 115 amu are also observed on-axis. Similar to the positive ion mass spectra, a background is observed at small angles that disappears at large angles. Since the background at both polarities appears at angles where the deposition meter registers a mass flow, and because the quadrupole mass filter does not discriminate against high m/q particles, the background can be attributed to droplets. As is also apparent in Figs. 3 and 4, at both polarities, the maximum ion current is registered off axis.

Fig. 5 shows the room temperature retarding potential curve for high-mass positive species produced on-axis. The distribution is obtained by recording charges transmitted through the mass filter in an rf-only mode in which the amplitude is set to transmit only high m/q particles (≥1200 amu). For this measurement the emitter was biased at 500 V. The insert chart is the corresponding energy distribution which is obtained from the derivative of the retarding potential curve, and exhibits a single

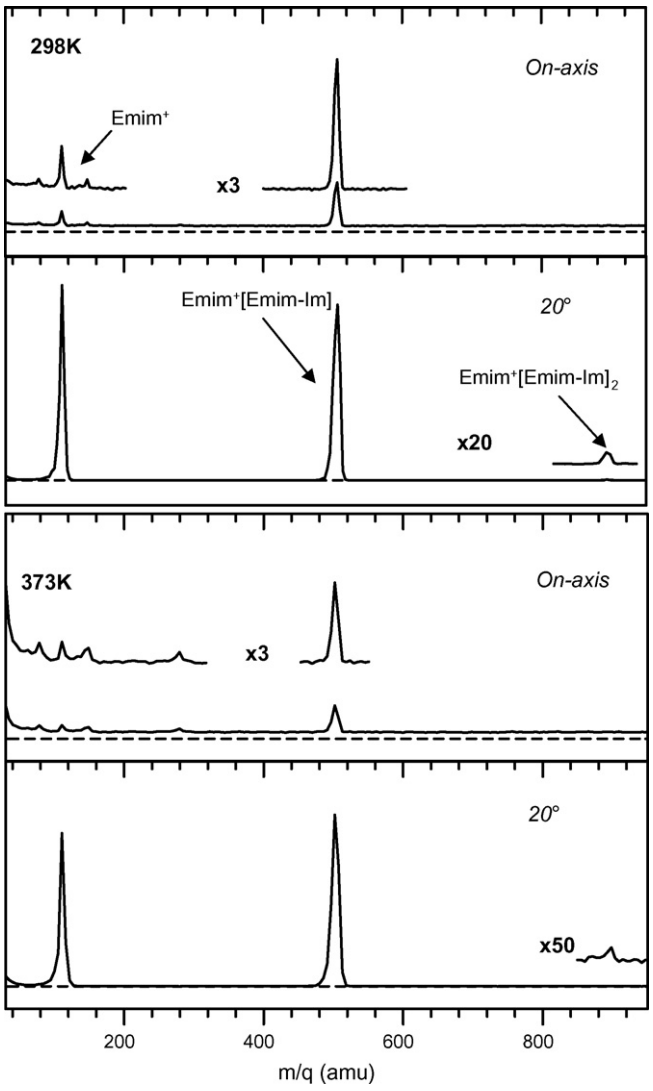

Fig. 3. Positive ion mass spectra as a function of emitter angle and temperature. On axis corresponds to the emitter aligned with the main instrument axis. The dashed lines represent zero intensity levels. All mass spectra are shown on the same vertical signal scale and were recorded for the same acquisition period.

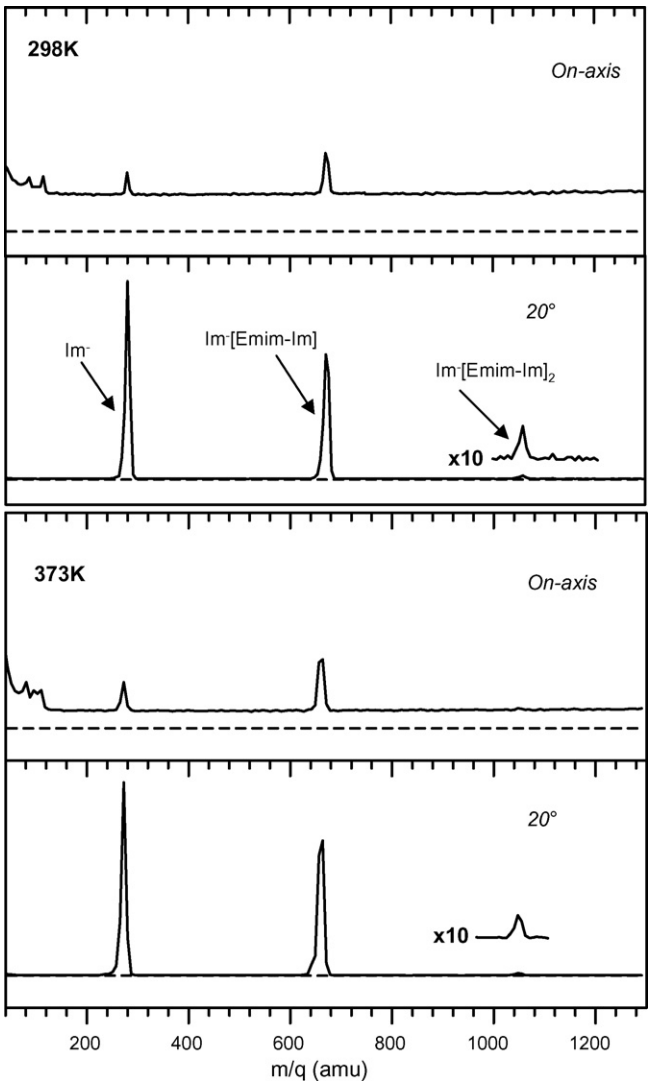

Fig. 4. Negative ion mass spectra as a function of emitter angle and temperature. On axis corresponds to the emitter aligned with the main instrument axis. The dashed lines represent zero intensity levels. All mass spectra are shown on the same vertical signal scale and were recorded for the same acquisition period.

broad peak centered at ∼320 eV per charge unit. The energy distributions of the $Emim^+$ ions recorded on-axis and at 18° are plotted in Fig. 6. Two peaks are observed in the energy distribution: one intense, narrow peak with a width of ∼30 eV centered at ∼500 eV and a weak peak centered at ∼280 eV. The energy distribution of the $Emim^+$[Emim][Im] ion is essentially identical.

The high-mass negative particles exhibit a similar broad energy distribution centered at 320 eV per charge unit as observed for the positive particles (Fig. 5). Fig. 7 shows the energy distributions of Im^- ions on-axis and at an angle of 20°. Similar to the $Emim^+$ axial energy distributions, a narrow band peaked at an energy corresponding to the emitter potential, as well as a weaker broader band around the energy observed for high-mass ions are observed. The large-angle ions are predominantly produced at 500 eV, while some evidence for slower ions around 300 eV is also apparent. Again, the larger Im^-[Emim][Im] ion has an energy distribution very similar to the monomer ion.

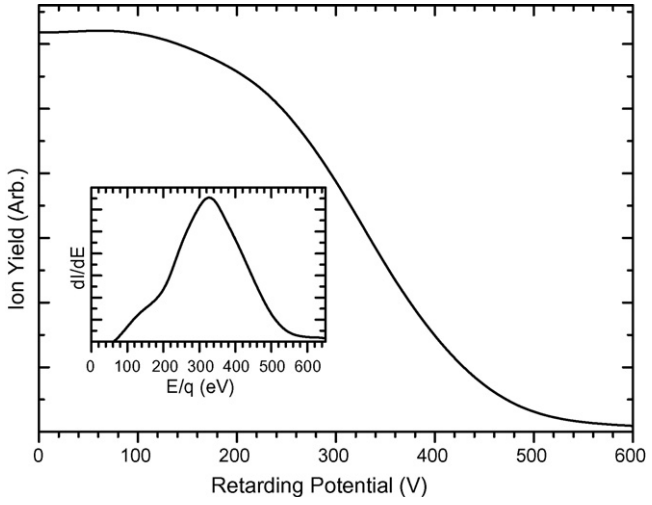

Fig. 5. The retarding potential curve measured for positive high *m/q* particles (*m/q* ≥ 1200 amu). The insert is the corresponding energy distribution per charge unit.

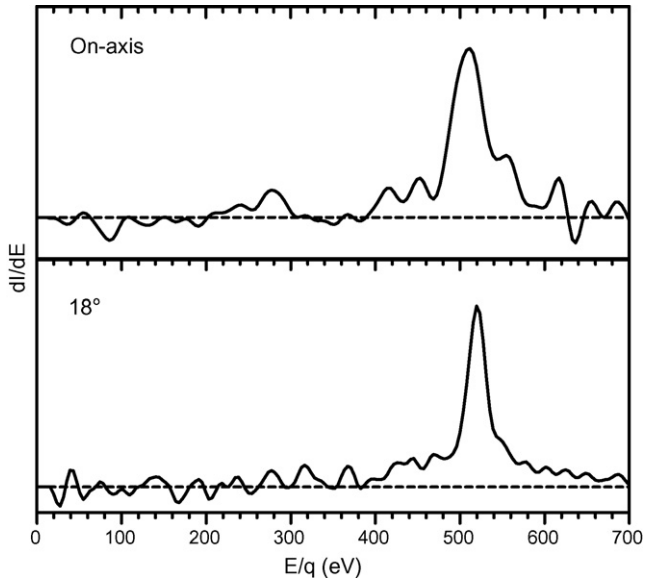

Fig. 6. Energy distributions of the $Emim^+$ ion recorded on-axis (top) and at 18° (bottom). The dashed lines correspond to zero signal level.

While the near-field target experimental data were obtained for very short continuous polarity periods, the measurements involving ion transmission through the quadrupole (Figs. 5–7) were all obtained in an alternating polarity mode (i.e., the respective data correspond to measurements gated during the respective polarity cycle). Without polarity alternation, the output current is found to be stable for a negative polarity, but results in a rapid decay of output current at a positive polarity. This is illustrated in Fig. 8, where the measured output current (square symbol) is plotted as a function of time. At $t = 0$, the electrospray source is switched from a stable alternating polarity (ac) mode to a continuous (dc) positive polarity mode. The dashed line indicates a first order exponential decay fit of the experimental data points.

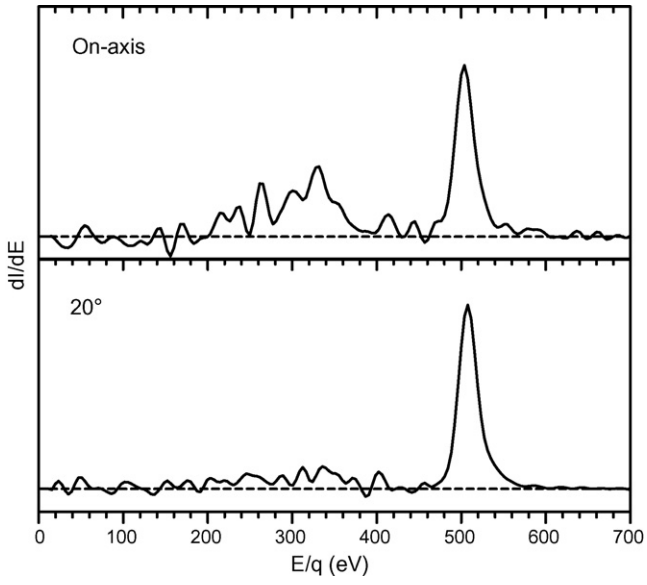

Fig. 7. Energy distributions of the Im^- ion recorded on-axis (top) and at 20° (bottom). The dashed lines correspond to zero signal level.

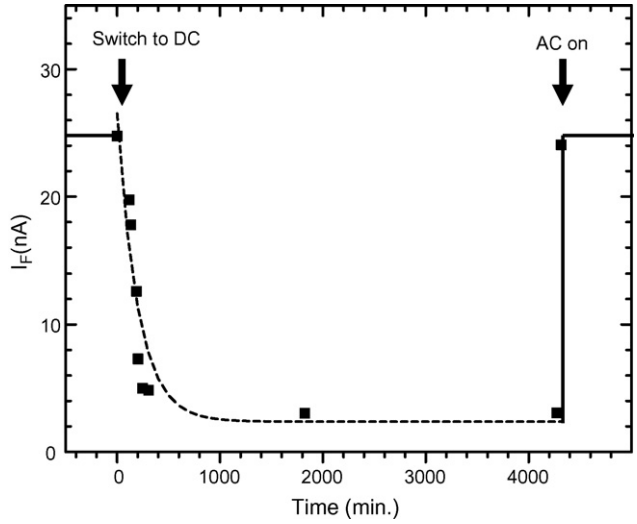

Fig. 8. Time dependence of the Faraday cup current for axial positive charge emission when switching from alternating polarity (ac) to continuous positive polarity (dc) operation and back.

The current decays from a current of ∼25 nA during the positive cycle to a constant current of 2–3 nA in ∼10 h. After approximately 3 days, the source is returned to an alternating polarity mode, and the current during the positive polarity cycle is almost instantaneously restored to its original value.

Fig. 9 shows the time evolution of positive-ion mass spectra during the same experiment of Fig. 8. The first spectrum was recorded prior to dc operation, the second at 247 min after initiation of dc operation, and the third after return to ac mode. Two new masses are seen at 391 and 783 amu in the 247 min spectrum. These lines appear approximately after 100 min of positive-only polarity operation, and are assigned to $Emim^+$-Im^0 and $Emim^+$-Im^0[Emim-Im], respectively. Simultaneously, the background attributable to droplets is also observed to decrease with time. The new ions, attributable to an association complex involving a neutralized Im^- ion, instantly disappear when switching back to the alternating polarity mode.

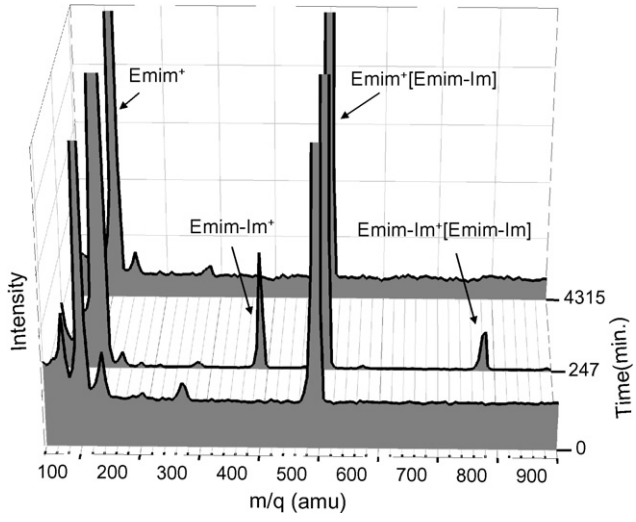

Fig. 9. Time evolution of positive ion mass spectra measured on-axis at the indicated times of the experiment shown in Fig. 8.

Table 2
B3LYP/6-311++G(d,p) predicted geometries of $Emim^0$ and $Emim^+$

Parameter	$Emim^0$	$Emim^+$
R(N1–C2)	1.393	1.382
R(C2–C4)	1.351	1.361
R(C4–N5)	1.395	1.382
R(N5–C3)	1.418	1.337
R(C3–N1)	1.416	1.338
R(N1–C7)	1.449	1.472
R(N5–C13)	1.459	1.485
R(C13–C14)	1.527	1.526
R(C2–H11)	1.078	1.077
R(C4–H12)	1.078	1.077
R(C3–H6)	1.089	1.078
R(C7–H8)	1.092	1.090
R(C7–H9)	1.092	1.088
R(C7–H10)	1.100	1.090
R(C13–H18)	1.101	1.091
R(C13–H19)	1.094	1.091
R(C14–H15)	1.094	1.092
R(C14–H16)	1.093	1.092
R(C14–H17)	1.093	1.092
α(N1–C3–N5)	105.0	109.0
α(C2–N1–C3)	107.8	108.4
α(C4–N5–C3)	107.5	108.3
α(N1–C2–C4)	108.6	107.1
α(N5–C4–C2)	108.9	107.2
α(C3–N1–C7)	121.0	125.9
α(C3–N5–C13)	121.4	125.7
α(N5–C13–C14)	112.7	112.4
α(H6–C3–N1)	117.4	125.5
α(H11–C2–N1)	121.7	122.2
α(H12–C4–N5)	121.6	122.2
τ(N1–C2–C4–N5)[a]	−0.1	−0.1
τ(C3–N1–C2–C4)[a]	9.2	0.0
τ(C3–N5–C4–C2)[a]	9.0	−0.2
ω(C7–N1–C3–C2)[b]	25.6	0.4
ω(C13–N5–C4–C3)[b]	27.4	−1.4
ω(H6–C3–N1–N5)[b]	39.6	−0.2
ω(H11–C2–C4–N1)[b]	3.1	−0.3
ω(H12–C4–N5–C2)[b]	3.0	−0.3

Bond lengths in Ångstroms; bond angles and dihedral angles in degrees. Refer to Figs. 10 and 11 for atomic numbering scheme.

[a] *τ*(A–B–C–D) denotes the dihedral angle between the planes containing atoms ABC and BCD.

[b] *ω*(A–B–C–D) denotes the dihedral angle between the A–B bond and the plane containing atoms BCD.

4.2. Quantum chemical calculations

The B3LYP/6-311++G(d,p) optimized geometries of $Emim^0$ and $Emim^+$ are summarized in Table 2. The bond lengths and interior bond angles in the planar five-membered N1–C2–C4–N5–C3 ring in $Emim^+$ are similar, ranging from 1.34 to 1.38 Å and 107 to 109°, respectively. The numbering schemes are shown in Fig. 10. The nearly symmetric pentagonal geometry of the ring suggests the presence of a delocalized (i.e., aromatic) π electron distribution, which is consistent with the π electron delocalization found in triazolium, tetrazolium, and pentazolium cations [33–35].

The structure of the five-membered ring in the neutral doublet $Emim^0$ radical, formed by the addition of an electron to $Emim^+$, shows significant deviation from the planar, pseudo-

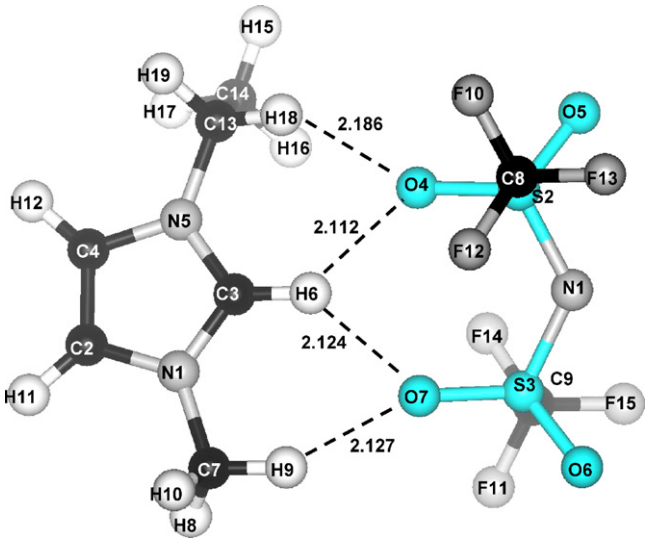

Fig. 10. B3LYP/6-311++G(d,p) geometry of [$Emim^+$][Im^-]-a. Interatomic distances are given in Ångstroms.

symmetric geometry found in $Emim^+$. In $Emim^0$, the N1–C3 and C3–N5 bond lengths are approximately 0.08 Å longer than those in $Emim^+$. A more subtle difference is seen in the N1–C7 and N5–C13 bond lengths, which are about 0.02 Å shorter in $Emim^0$ relative to $Emim^+$. The $Emim^0$ ring is slightly puckered about atom C3, with C3–N1–C2–C4 and C3–N5–C4–C2 dihedral angles of about 9°.

The increase in the N1–C3 and C3–N5 bond lengths relative to those in $Emim^+$ is consistent with reduced double-bond character in these bonds. Furthermore, the pyramidalization of N1 (N5), as shown in Table 2 by the angle of 26° (27°) between the N1–C7 (N5–C13) bond and the plane containing atoms C3–N1–C2 (C3–N5–C4), suggests partial localization of a lone pair on this atom. Similarly, the pyramidalization of C3, shown by the 40° angle between the C3–H6 bond and the plane containing N1–C3–N5, indicates the localization of the unpaired electron on this atom. The lengthening of the N1–C3 and C3–N5 bonds, the localization of lone electron pairs on N1 and N5, the localization of the unpaired electron on C3, and the non-planarity of the five-membered ring are all consistent with a diminished degree of π electron delocalization (i.e., aromaticity) relative to $Emim^+$. Finally, a Löwdin population analysis of $Emim^0$ shows that the unpaired electron is primarily centered on C3 (atomic spin population of 0.46 electrons), but with some residual populations on N1 and N5 (0.15 and 0.14 electrons, respectively).

The calculated geometries of Im^0 and Im^- are given in Table 3. Although the point group symmetry of the Im^- anion is strictly C_1, the geometry is approximately C_2, with the two-fold rotation axis passing through the nitrogen atom and lying in the S2–N1–S3 plane. The geometry of Im^0 is likewise strictly C_1 but has an approximate C_s symmetry plane containing atoms C8–S2–N1–S3–C9. Another primary difference between the geometries of Im^- and Im^0 is the lengthening of the N1–S2 and N1–S3 bonds in the latter by 0.08 Å. A Löwdin population analysis of Im^0 indicates the unpaired electron is localized on the nitrogen atom (atomic spin populaton of 0.69 electrons).

Table 3
B3LYP/6-311++G(d,p) predicted geometries of Im^0 and Im^-

Parameter	Im^0	Im^-
R(N1–S2)	1.691	1.613
R(N1–S3)	1.694	1.613
R(S2–O4)	1.450	1.462
R(S2–O5)	1.451	1.462
R(S3–O6)	1.447	1.462
R(S3–O7)	1.450	1.462
R(S2–C8)	1.902	1.895
R(S3–C9)	1.912	1.895
R(C8–F10)	1.329	1.347
R(C8–F12)	1.324	1.339
R(C8–F13)	1.325	1.341
R(C9–F11)	1.326	1.347
R(C9–F14)	1.327	1.339
R(C9–F15)	1.323	1.341
α(S2–N1–S3)	129.7	126.3
α(N1–S2–O4)	109.1	117.3
α(N1–S2–O5)	110.0	108.3
α(O4–S2–O5)	122.9	119.0
α(N1–S3–O6)	105.1	108.3
α(N1–S3–O7)	104.9	117.3
α(O6–S3–O7)	123.4	119.0
α(N1–S2–C8)	96.4	102.2
α(N1–S3–C9)	109.7	102.2
α(S2–C8–F10)	106.8	109.7
α(S2–C8–F12)	109.9	111.6
α(S2–C8–F13)	109.8	111.5
α(S3–C9–F11)	106.7	109.7
α(S3–C9–F14)	108.9	111.6
α(S3–C9–F15)	109.7	111.4
τ(S3–N1–S2–C8)[a]	179.7	94.4
τ(S2–N1–S3–C9)[a]	18.5	94.7
τ(N1–S2–C8–F10)[a]	179.5	179.5
τ(N1–S3–C9–F11)[a]	−173.6	179.3

Bond lengths in Ångstroms; bond angles and dihedral angles in degrees. Refer to Figs. 10 and 11 for atomic numbering scheme.

[a] τ(A–B–C–D) denotes the dihedral angle between the planes containing atoms ABC and BCD.

Two distinct local minima were found for the parent [Emim][Im] ion pair, denoted as "[Emim][Im]-a" and "[Emim][Im]-b", which are illustrated in Figs. 10 and 11, respectively. The essential difference between the two minima is that the $Emim^+$ cation is located on opposite "sides" of the Im^- anion. In [Emim][Im]-a, there are four O–H interionic hydrogen bonds between the O4 and O7 oxygen atoms on Im^- and the H6, H9, and H18 hydrogen atoms on $Emim^+$, with bond lengths ranging from 2.11 to 2.19 Å. In contrast, [Emim][Im]-b has two O–H hydrogen bonds (O5–H18 and O6–H9, with bond lengths of 2.21 and 2.11 Å, respectively) and a strong N1–H6 hydrogen bond (1.99 Å).

The geometry of the Im^-[Emim][Im] ion cluster is shown in Fig. 12. The hydrogen bonding interactions between $Emim^+$ and the Im^- anion to the right of the cation are similar to those present in the [Emim][Im]-a ion pair, although the bond lengths are somewhat longer in the former, ranging from 2.14 to 2.34 Å. The second Im^- anion, located on the left side of the cation, forms a relatively strong hydrogen bond between O6′ and H12 (2.11 Å) and a weaker bond between O7′ and H19 (2.56 Å).

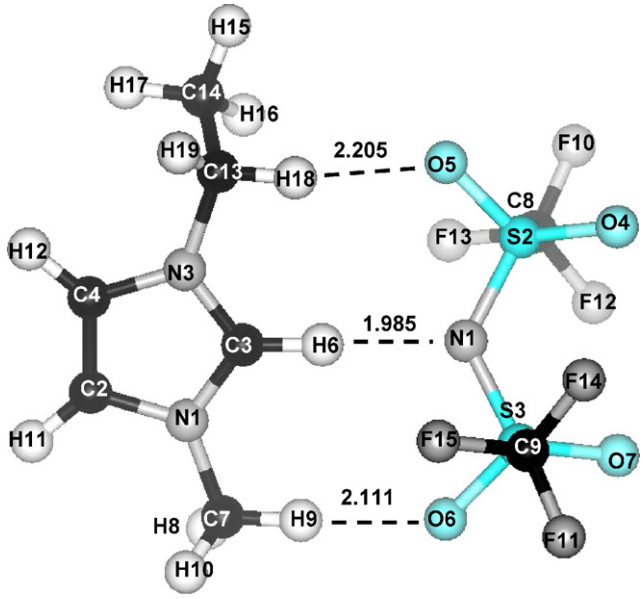

Fig. 11. B3LYP/6-311++G(d,p) geometry of [$Emim^+$][Im^-]-b. Interatomic distances are given in Ångstroms.

The structure of the $Emim^+$[Emim][Im] cluster is illustrated in Fig. 13. The interactions between Im^- and the $Emim^+$ cation located to the right of the anion are analogous to those present in the [Emim][Im]-b ion pair (see Fig. 11), although each of the individual hydrogen bond lengths, which range from 2.10 to 2.36 Å, are longer relative to the latter. Similarly, the hydrogen bonds formed between the Im^- anion and $Emim^+$ located to the left of the anion closely resemble those found in [Emim][Im]-a (see Fig. 10), but likewise are consistently longer, ranging from 2.23 to 2.27 Å.

The binding enthalpies of the ion clusters are summarized in Table 4. Note that the B3LYP/6-311++G(d,p) harmonic vibrational frequencies used to compute the zero-point vibrational energy corrections have been scaled by a factor of 0.9806 [36]. Relative to separated $Emim^+$ and Im^- ions, the [Emim][Im]-a and [Emim][Im]-b ion pairs are bound by approximately 315 and

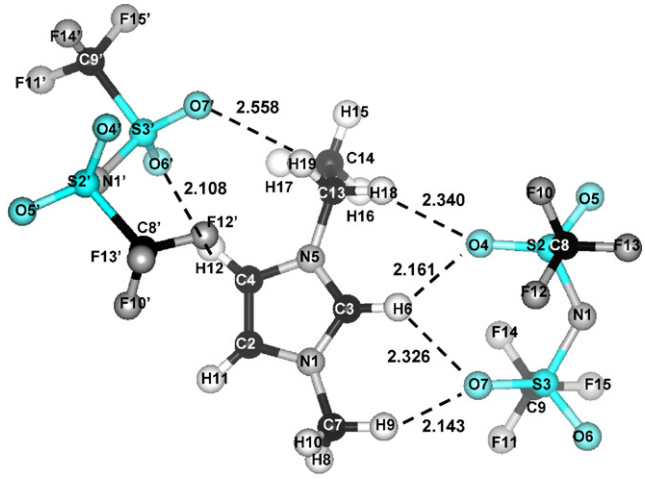

Fig. 12. B3LYP/6-311++G(d,p) geometry of Im^-[Emim][Im]. Interatomic distances are given in Ångstroms.

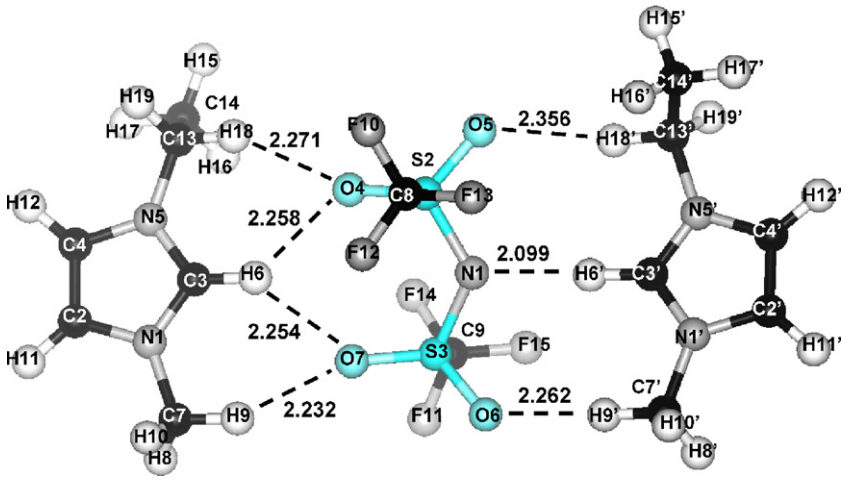

Fig. 13. B3LYP/6-311++G(d,p) geometry of $Emim^+[Emim][Im]$. Interatomic distances are given in Ångstroms.

Table 4
B3LYP/6-311++G(d,p) total energies, zero-point vibrational (ZPV) energies, and 0 K binding enthalpies ($\Delta H(0\,K)$) of $(Emim)_m(Im)_n$ clusters ($0 \le m, n \le 2$)

Species	Total energy (Hartrees)	ZPV energy[a] (kJ/mol)	$\Delta H(0\,K)$ (kJ/mol)
$Emim^0$	−344.555828	422.6	n/a
$Emim^+$	−344.416337	433.1	n/a
Im^0	−1826.883159	131.1	n/a
Im^-	−1827.087332	133.9	n/a
$(Emim^+)(Im^-)$ "a"	−2171.624964	570.6	314.9[b]
$(Emim^+)(Im^-)$ "b"	−2171.625635	570.8	316.4[b]
$Im^-[Emim][Im]$	−3998.746236	707.1	86.6[c]
$Emim^+[Emim][Im]$	−2516.089211	1007.2	122.3[c]

[a] Harmonic frequencies used to compute the ZPV energies have been scaled by 0.9806 [36].
[b] Relative to $Emim^+ + Im^-$.
[c] Relative to $X^\pm + (Emim^+)(Im^-)$, X = Emim, Im.

316 kJ/mol (0 K), respectively. Relative to separated Im^- plus the ion pair [Emim][Im], the $Im^-[Emim][Im]$ cluster is more stable by 87 kJ/mol (0 K). The $Emim^+[Emim][Im]$ ion cluster is more stable relative to separated $Emim^+$ plus [Emim][Im] by 122 kJ/mol (0 K). Therefore, it is energetically more favorable by 35 kJ/mol to add a second cation, rather than another anion, to the [Emim][Im] ion pair.

In relation to the ion clusters observed in the ESI mass spectra and the associated temperature dependence, it is worth examining the stability of the observed clusters at the source temperatures. Fig. 14 plots the internal energy distributions of the $Emim^+[Emim][Im]$ and $Im^-[Emim][Im]$ cluster ions at the two investigated source temperatures. The internal energy distributions are determined from:

$$F(E_{int})\,dE_{int} = F_{rot}(E_{rot})F_{vib}(E_{vib})\,dE_{rot}\,dE_{vib} \quad (3)$$

where $F_{rot}(E_{rot})$ and $F_{vib}(E_{vib})$ are the normalized rotational and vibrational Maxwell–Boltzmann energy distribution functions for a temperature, T, and:

$$E_{int} = E_{rot} + E_{vib}. \quad (4)$$

The vibrational energy is determined from the scaled frequencies determined for the global minima of the potential energy surface. A harmonic approximation is assumed for excited vibrational levels. The vertical dashed lines in Fig. 14 indicate the 0 K dissociation thresholds. In the case of the positive ion, approximately 5% of ions are produced above the dissociation threshold at 298 K, increasing to 65% at 373 K. The internal energy of the negative ions is slightly higher, however, due to the lower threshold, a considerably higher thermal dissociation fraction results: ~87% at 298 K, and 98% at 373 K.

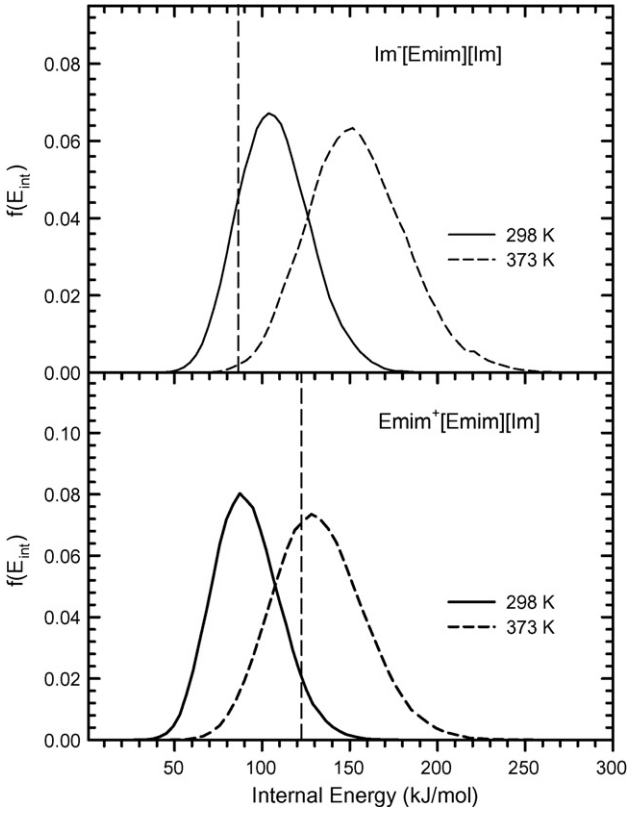

Fig. 14. Calculated thermal internal energy distributions at 298 and 373 K for $Im^-[Emim][Im]$ (top) and $Emim^+[Emim][Im]$ (bottom). The vertical dashed lines represent the dissociation limits of the respective cluster ions.

5. Discussion

The present work investigates the electrohydrodynamic and mass spectral properties of stable cone–jets formed with the ionic liquid, [Emim][Im], wetted on a sharp tungsten needle. The near-field target measurements and derived critical dimensions and fields listed in Table 1 show that the presently investigated jets take on nanodimensions, and that the derived surface field strengths fall into the regime where ion field evaporation is possible. Interestingly, the absolute field strengths are at the low end of a range of 0.7–2.5 V/nm determined for solutions by several groups [13–15]. Ion field evaporation becomes clearly evident in the near-field angular distributions shown in Fig. 2. Field-evaporated ions are evidenced for both polarities by a sizeable current at large angles where there is negligible mass flow. This observation is independent of source temperature.

Furthermore, the near-field target measurements indicate that the dimensions and the surface electric field of the critical regions of the cone–jet do not change significantly when raising the source temperature from room temperature to 373 K. This implies, upon inspection of Eqs. (1) and (2), that temperature increases the conductivity and mass flow almost equally. A significant increase in mass flow and to a lesser degree current with temperature is observed. This is consistent with the proportionality determined by Fernández de la Mora and Loscertales for a Taylor cone of a conducting liquid [37]:

$$I \sim \left(\frac{\gamma K Q}{\varepsilon}\right)^{1/2}, \tag{5}$$

where ε is the dielectric constant. Interestingly, while the apparent dimensions predicted by Eqs. (1) and (2) of the jet/neck region do not increase, the average mass-to-charge ratio of the observed droplets, as derived from the measured mass flow and currents, is seen to increase in Table 1 with temperature. Assuming that the drops are formed with charge close to the Rayleigh limit, q_R, where Coulombic repulsion balances the capillary forces associated with surface tension [38]:

$$q_R = (8\pi^2 \varepsilon_0 \gamma d^3)^{1/2}, \tag{6}$$

larger average mass-to-charge ratios signify larger droplets. Thus, it appears that heating the jet leads to larger flow rates due to the lower viscosity of the ionic liquid, which results in higher jet speeds while not significantly altering the jet diameter. A higher jet speed signifies lower charge density, however. Consequently, in the high-temperature case, droplet pinch off must happen closer to the neck, producing more elongated droplets.

Interestingly, Romero-Sanz et al. report a temperature dependent study of ionic liquid Taylor cones formed from a pressure-driven capillary that shows the opposite behavior, where the droplet size is seen to decrease to the point of pure ion emission as the temperature increases [39]. In that study, the goal was to reach a purely ionic regime by controlling the liquid flow rate, Q, in the capillary. Thus, in the work by Romero-Sanz et al., it is the reduction of the surface tension, γ, that leads to the size reduction and ultimate elimination of emitted droplets. In the case of the present externally wetted emitters, it appears to be the change in electrohydrodynamic regime with temperature that dictates the cone–jet dynamics.

More detailed information on the atomistic physics of the present ionic liquid cone–jets can be obtained in the mass spectral measurements. They fully confirm the picture provided by the near-field angular measurements in Fig. 2, where nearly pure ion emission is observed at large angles, while at small emission angles with respect to the needle axis, droplet emission, evidenced by a mass-independent background, is important. At $\sim 20^\circ$ the main ions are $X^{\pm}\{[Emim][Im]\}_n$, $n = 0$, 1, where X is $Emim^+$ or Im^-, depending on the polarity of the electrospray source. Similar intensities are observed for $n = 0$ and 1, while only minor signals are observed for $n = 2$ cluster ions. On axis, the $n = 1$ clusters have significantly higher relative intensities in comparison with $n = 0$, and there is no evidence for $n = 2$ clusters.

When comparing the positive and negative ion mass spectra, it can be seen that the relative intensity of the positive $n = 1$ cluster ion is higher than that of the corresponding negative cluster ion both on and off axis. This could be related to the higher binding energy of the former, as well as the higher internal energies of the latter. The present quantum chemical calculations indicate that the $n = 1$ cluster ions have internal energies close to their respective dissociation limits (see Fig. 14). The $n = 2$ cluster ions, therefore, can be expected to be thermally unstable given the larger number of low-frequency modes, and the expected similar, if not lower dissociation thresholds. This could explain the low intensity of $n = 2$ species.

Vacuum ESI studies on NaI/formamide solutions [17,40] indicated that positive solvated ion distributions were governed by thermal stability, exhibiting a sharp decline above solvation numbers found to be thermally unstable. As the distributions in Fig. 14 demonstrate, however, the present structure and normal frequency calculations predict more than 90% of Im^-[Emim][Im] to be thermally dissociated at 373 K. The mass spectra do not show any significant decrease in Im^-[Emim][Im] intensity with respect to the significantly more stable Im^- ion as the temperature is increased. As evidenced by the weak Im^-[Emim][Im]$_2$ intensities, larger, thermally unstable cluster ions are emitted from the cone–jet. It is thus conceivable that a large fraction of the Im^-[Emim][Im] ions result from the decay of larger cluster ions following rapid multiple losses of [Emim][Im] ion pairs, thereby stabilizing the cluster through evaporative cooling. Another possibility is that the dissociation dynamics are highly constrained in these cluster ions with multiple coordination sites as evidenced by the derived equilibrium structures. Molecular dynamics simulations of thermally dissociating cluster ions and the associated dissociation rates could shed more light on this. Similar arguments can be made with the analogous observations for the positive ions. Evidence for evaporative cooling has also been observed in the aforementioned vacuum ESI studies on NaI/formamide solutions [17,40].

The field-evaporated ions can have multiple origins: the jet neck region, as suggested by Gamero-Castaño and Fernández de la Mora [12,16]; the tip of the jet where small interface curvatures also arise, or from emitted, super-charged droplets. The mass-resolved energy distribution measurements show that the droplets are formed at a region of the cone–jet that has a poten-

tial approximately 200 V below the 500 V needle bias voltage. This implies ohmic losses, which are most likely to occur in the transition neck region of the cone–jet prior to convective flow in the jet. The ion energy distributions, shown in Figs. 6 and 7, peak at high energies corresponding to field evaporation in regions of the cone–jet upstream from where ohmic losses occur. This is clear evidence that ion emission occurs primarily from locations of the neck-transition region where the liquid potential is still almost identical to the needle potential. The peaking of ion field-evaporation currents off axis can then be understood as being related to the initial acceleration off axis by the surface normal fields at the liquid vacuum interface (see Fig. 1). In the energy distribution of Im^-, a second peak near the droplet energy is discernable at 20°, suggesting that some ions are produced at points of lower potential, i.e., the transition region downstream from the location of ohmic losses, or the jet tip, or from droplets.

The present ion energy distributions peaking at energies corresponding to formation at a potential within ∼10 V of the needle potential are consistent with higher accuracy energy measurements by Lozano [41], who observed from similar [Emim][Im] wetted tungsten needle studies energy deficits of a few electronvolts with respect to the applied needle potential. While Lozano's source was operated with voltages ranging from ±900 to ±1200 V, close to the present operating voltage, his needle emitted only ions. The precise emission conditions are closely related to the microscopic needle geometry and wetting properties. It must, therefore, be assumed that the difference between the present work and that of Lozano is related to the smaller needle tip curvature of 5–10 μm reported by Lozano, while the curvature of the needle of the present study is around 20 μm.

The present evidence of [Emim][Im] ion field evaporation at the jet neck of a cone–jet is consistent with continuum hydrodynamic predictions [12,16]. However, it contrasts with recent work on NaI/formamide solutions electrosprayed in a mixed ion-droplet regime [16,17,40], where field evaporated ions exhibited energies symptomatic of emission at the jet tip. The present results imply that there is no fundamental problem with the theory, and that the solution, unlike the present ionic liquid, may not have the electrostatic continuum fluid properties that the theory is based on. In case of the solution, similar dimensions and higher surface normal fields are derived [40]. Thus, it can be imagined that the jet or neck dimensions are reduced to the point that the associated volume has only a small number of ions at the given concentration, making the surface charge at the neck ill-defined and highly fluctuating. A discretization of surface charge in solutions has previously been proposed by Fenn, as communicated by Loscertales and Fernández de la Mora [13], whereby the latter authors have presented arguments based on continuum models against this idea. Recent molecular dynamics simulations of a NaI/formamide droplet in a uniform electric field, however, high-light the importance of the polar solvent in establishing the surface-normal field, and demonstrate highly fluctuating charge densities in the neck region, with all field-evaporating ions occurring at the tips of jets formed from the droplet surface [40].

The present ionic liquid, when operated in a dc polarity mode, exhibits interesting electrochemical effects. The negative spray appears stable with no alteration of the mass spectrum over long periods of time (hours). When operated at a positive polarity, the output current is observed to progressively decay, with an eventual appearance of new mass peaks associated with $Emim^+([Emim][Im])_n$ ions bound to what could be the neutralized negative ion. This would be consistent with an electrochemical electron detachment of the anion at the tungsten-ionic liquid interface. Although our mass resolution cannot positively identify the mass of the new ions, the fact that Im^0 does not contain hydrogen atoms allows us to resolve any possible Im^0 fragments. If the new ions in fact correspond to electrochemical decay ions, one is tempted to assume that the reduction in total emission current is related to electrochemical transformation of the liquid properties. The significant accumulation of electrochemical reaction products, which should correlate with the number of emitted charges, would be expected to result in a persistence of electrochemical product ion emission following the return to ac operation.

The sudden disappearance of the associated peaks, and the simultaneous instantaneous recovery of the emission current, calls for an alternate explanation. The observations suggest that the electrochemical transformation of the emitter-ionic liquid interfacial properties are throttling the flow of the ionic liquid across the emitter surface, resulting in reduced emission currents. Reduced flow could result from the generation of an immobilized ionic liquid phase layer that is in contact with the tungsten surface of the emitter. During the formation of the electrochemical double layer, a layer with surplus in negative charge forms at the liquid–metal interface. From estimates of the capacitance associated with the double layer, it has been shown for externally wetted ESI sources of the present dimensions that it takes on the order of seconds for this double layer to form [22]. Once the layer has formed, it can be imagined that an additional layer with surplus of positive charge will immobilize on top of the interfacial liquid layer. A continued steady build-up of charge layers with alternating polarities in the liquid, immobilized by the strong attraction, would eventually lead to noticeable flow resistance as the mobile, liquid phase of the thin film grows thinner and thinner. Once the polarity is reversed, the built-up interfacial structure disintegrates, and the layering of a new stack is initiated starting with the opposite polarity. Indeed, "quasi-ternary layers" have been proposed to clarify the capacitive behavior of imidazolium-based ionic liquids [42]. The same study also found evidence for bulky, rough interface layers due to ionic cluster pairs, fully consistent with the present interpretation as well as the observed ionic clusters.

Other interfacial phenomena related to the present observation have been reported. Increased ordering of liquid crystal boundary layers caused by a crystal alignment by the substrate potential has been discussed theoretically by Sheng [43]. Polar ordering of water molecules extending ∼30 monolayers in thin ice films has been measured on Pt(1 1 1), and proposed to result from the strong interfacial water–metal dipole-induced interaction. While that work involved a well-characterized single-crystal metal surface and a temperature below 137 K, the present effects are associated with a rough tungsten surface at room temperature [44].

The present interpretation, of considerable hypothetical nature, still requires an explanation as to what happens to the electrochemical products and why the dc operation only appears to affect positive charge emission. In case of positive polarity, if the neutralized Im^- ions do not fragment, it is possible that electrons can easily transfer from an Im^- of a neighboring layer to the Im^0 formed at the interface. Similar electron transfer reactions could continue to occur until an anion is neutralized at the top of the immobilized ion stack, where the flow can carry it towards the point of emission. It is not fully clear why in the case of negative polarity, neither the current suppression nor electrochemical biproducts are observed. The present quantum chemical calculations show that neutralized $Emim^0$ products lose their aromaticity, and it is possible that the neutralized ions fragment at the cathode interface. Experiments on [Emim][BF_4] [22] have shown bubble formation at the cathode of an electrochemical cell, as well as on a wetted tungsten emitter, consistent with electrochemical decay of the $Emim^+$ ions to neutral, gaseous products. This would also be consistent with the lack of electrochemical decay products observed in the mass spectrum. Bubble formation would also perturb the formation of an immobilized ionic liquid film. Present efforts at identifying bubbles using a video microscope were unsuccessful, raising the possibility that the produced bubbles were very small.

6. Conclusions

A detailed analysis is presented of the electrohydrodynamics and mass spectra of vacuum electrospray currents extracted from a sharp tungsten tip etched from a 500 μm wire and wetted with the ionic liquid, [Emim][Im]. The source is operated at a low extraction voltage of approximately ±1 kV, at which conditions the ESI source operates in a cone–jet configuration. The polarity of the emitter is alternated at a frequency of 1 Hz to suppress electrochemical effects. Angular distributions of current and mass flow reveal that at small emission angles with respect to the needle axis, primarily droplets are emitted, while at large angles, the current is dominated by field evaporated ions. A mass spectrometric analysis of electrospray current reveals primarily $X^{\pm}\{[Emim][Im]\}_n$ ions (X = Emim or Im for positive and negative polarities, respectively) with $n = 0$, 1, and 2. Minor trace ions are also observed. Quantum chemical calculations indicate that the $n = 1$ ions have thermal energies near or above the dissociation limit at the temperatures of the present experiments. The lack of a dependence of the observed mass spectra on temperature suggest that the observed $n = 1$ and 2 ions could be the products of thermally dissociated ions of higher coordination numbers, n, and are stable due to an evaporative cooling mechanism.

The angular distributions and the mass-resolved energy distributions of ions and droplets are consistent with theoretical predictions [12,16] that ion field evaporation occurs at the cone–jet neck region, while droplet formation occurs at the tip of the jet. Raising the temperature of the ionic liquid to 373 K increases the mass flow significantly, implying larger droplets. This can be attributed to the lower viscosity at higher temperatures, and the consequent higher liquid flow rates on the needle surface. Electrochemical modification and degradation of the cone–jet emitter properties are observed when maintaining the emitter at a positive polarity for a prolonged (minutes to hours) period. The emission current is severely suppressed, while new ions are observed in the mass spectrum of the emitted ion current. Return to a polarity alternation mode instantaneously restores the current and mass spectrum. The degradation is associated with the formation of a growing stack of immobilized, polarity alternating liquid layers on the tungsten–ionic liquid interface. In case of negative charge emission, dc operation does not lead to noticeable degradation of the emitter performance. This could be explained with the formation of volatile electrochemical reaction products.

Acknowledgements

The authors acknowledge many helpful discussions with Ramona Taylor, Professors Lozano and Martinez-Sanchez. We are particularly indebted to Professor Fernández de la Mora for many important comments pertaining to this manuscript. The authors are grateful for the support by the Air Force Office of Scientific Research under task 2303ES02 and the Space Miniaturization Theme (Program Manager: Michael R. Berman). The authors gratefully acknowledge grants of computer time from the DoD High Performance Computing Modernization Program at the Engineer Research and Development Center, the Army Research Laboratory, and the Aeronautical Systems Center.

References

[1] J.V. Iribarne, B.A. Thomson, J. Chem. Phys. 64 (1976) 2287.
[2] B.A. Thomson, J.V. Iribarne, J. Chem. Phys. 71 (1979) 4451.
[3] J.B. Fenn, M. Mann, C.K. Meng, S.F. Wong, C.M. Whitehouse, Science 246 (1989) 64.
[4] M.N. Huberman, J. Appl. Phys. 41 (1970) 578.
[5] D.S. Simons, B.N. Colby, C.A. Evans, Int. J. Mass Spectrom. Ion Phys. 15 (1974) 291.
[6] B.P. Stimpson, D.S. Simons, C.A. Evans, J. Phys. Chem. 82 (1978) 660.
[7] M. Martinez-Sanchez, J.E. Pollard, J. Prop. Power 14 (1998) 688.
[8] D.H. Reneker, I. Chun, Nanotechnology 7 (1996) 216.
[9] I.G. Loscertales, A. Barrero, I. Guerrero, R. Cortijo, M. Marquez, A.M. Gañan-Calvo, Science 295 (2002) 1695.
[10] M. Cloupeau, B. Prunet-Foch, J. Aerosol Sci. 25 (1994) 1021.
[11] G.I. Taylor, Proc. R. Soc. London A 280 (1964) 383.
[12] M. Gamero-Castaño, J. Fernández de la Mora, J. Chem. Phys. 113 (2000) 815.
[13] I.G. Loscertales, J. Fernández de la Mora, J. Chem. Phys. 103 (1995) 5041.
[14] V. Katta, A.L. Rockwood, M.L. Vestal, Int. J. Mass Spectrom. Ion Process. 103 (1991) 129.
[15] J.B. Fenn, J. Rosell, C.K. Meng, J. Am. Soc. Mass Spectrom. 8 (1997) 1147.
[16] M. Gamero-Castaño, Phys. Rev. Lett. 89 (2002) 147602.
[17] Y. Chiu, B.L. Austin, R.A. Dressler, D.J. Levandier, P.T. Murray, P. Lozano, M. Martinez-Sanchez, J. Prop. Power 21 (2005) 416.
[18] I. Romero-Sanz, R. Bocanegra, J. Fernandez de la Mora, M. Gamero-Castano, J. Appl. Phys. 94 (2003) 3599.
[19] J.K. Ziemer, M. Gamero-Castaño, V. Hruby, D. Spence, N. Demmons, R. McCormick, T. Roy, C. Gasdaska, J. Young, B. Connolly, AIAA 2005-4265, 41st AIAA/ASME/SAE/ASEE Joint Propulsion Conference and Exhibit, Tucson, Arizona, July, 2005.
[20] P. Lozano, M. Martinez-Sanchez, J. Colloids Interface Sci. 282 (2005) 415.

[21] Y. Chiu, G. Gaeta, T.R. Heine, R.A. Dressler, AIAA 2006-5010, 42nd AIAA/ASME/SAE/ASEE Joint Propulsion Conference & Exhibit, Sacramento, CA, July, 2006.
[22] P. Lozano, M. Martinez-Sanchez, J. Colloids Interface Sci. 280 (2004) 149.
[23] A.D. Becke, J. Chem. Phys. 98 (1993) 5648.
[24] R.H. Hertwig, W. Koch, Chem. Phys. Lett. 268 (1997) 345.
[25] P.J. Stephens, F.J. Devlin, C.F. Chabalowski, M.J. Frisch, J. Phys. Chem. 98 (1994) 11623.
[26] S.H. Vosko, L. Wilk, M. Nusair, Can. J. Phys. 58 (1980) 1200.
[27] T. Clark, J. Chandrasekhar, G.W. Spitznagel, P.V.R. Schleyer, J. Comput. Chem. 4 (1983) 294.
[28] P.C. Hariharan, J.A. Pople, Theor. Chim. Acta 28 (1973) 213.
[29] R. Krishnan, J.S. Binkley, R. Seeger, J.A. Pople, J. Chem. Phys. 72 (1980) 650.
[30] M.S. Gordon, M.W. Schmidt, in: C.E. Dykstra, G. Frenking, K.S. Kim, G.E. Scuseria (Eds.), Advances in Electronic Structure Theory: GAMESS a Decade Later, Elsevier, Amsterdam, 2005.
[31] M.W. Schmidt, K.K. Baldridge, J.A. Boatz, S.T. Elbert, M.S. Gordon, J.H. Jensen, S. Koseki, N. Matsunaga, K.A. Nguyen, S. Su, T.L. Windus, M. Dupuis, J.A. Montgomery Jr., J. Comput. Chem. 14 (1993) 1347.
[32] W. Martino, J. Fernández de la Mora, Y. Yoshida, G. Saito, J. Wilkes, Green Chem. 8 (2006) 390.
[33] I.S.O. Pimienta, S. Elzey, J.A. Boatz, M.S. Gordon, J. Phys. Chem. A 111 (2007) 691.
[34] M.W. Schmidt, M.S. Gordon, J.A. Boatz, J. Phys. Chem. A 109 (2005) 7285.
[35] D.D. Zorn, J.A. Boatz, M.S. Gordon, J. Phys. Chem. B 110 (2006) 11110.
[36] A.P. Scott, L. Radom, J. Phys. Chem. 100 (1996) 16502.
[37] J. Fernández de la Mora, I.G. Loscertales, J. Fluid Mech. 260 (1994) 155.
[38] L. Rayleigh, Philos. Mag. 14 (1882) 184.
[39] I. Romero-Sanz, I.A.d. Carcer, J. Fernandez de la Mora, J. Prop. Power 21 (2005) 239.
[40] Y. Chiu, R.A. Dressler, D. Luedtke, U. Landman, S. Sok, M.S. Gordon, in preparation.
[41] P. Lozano, J. Phys. D 39 (2006) 126.
[42] H. Liu, P. He, Z. Li, Y. Liu, J. Li, L. Zheng, J. Li, Electrochem. Solid-State Lett. 8 (2005) J17.
[43] P. Sheng, Phys. Rev. A 26 (1982) 1610.
[44] X. Su, L. Lianos, Y.R. Shen, G.A. Somorjai, Phys. Rev. Lett. 80 (1998) 1533.